Direct Observation of Wave-Coherent Pressure Work in the Atmospheric Boundary Layer

SETH F. ZIPPEL,[a,b] JAMES B. EDSON,[b] MALCOLM E. SCULLY,[b] AND OAKLIN R. KEEFE[b]

[a] College of Earth, Ocean, and Atmospheric Sciences, Oregon State University, Corvallis, Oregon
[b] Woods Hole Oceanographic Institution, Woods Hole, Massachusetts

(Manuscript received 2 June 2023, in final form 29 November 2023, accepted 1 December 2023)

ABSTRACT: Surface waves grow through a mechanism in which atmospheric pressure is offset in phase from the wavy surface. A pattern of low atmospheric pressure over upward wave orbital motions (leeward side) and high pressure over downward wave orbital motions (windward side) travels with the water wave, leading to a pumping of kinetic energy from the atmospheric boundary layer into the waves. This pressure pattern persists above the air–water interface, modifying the turbulent kinetic energy in the atmospheric wave-affected boundary layer. Here, we present field measurements of wave-coherent atmospheric pressure and velocity to elucidate the transfer of energy from the atmospheric turbulence budget into waves through wave-coherent atmospheric pressure work. Measurements show that the phase between wave-coherent pressure and velocity is shifted slightly above 90° when wind speed exceeds the wave phase speed, allowing for a downward energy flux via pressure work. Although previous studies have reported wave-coherent pressure, to the authors' knowledge, these are the first reported field measurements of wave-coherent pressure work. Measured pressure work cospectra are consistent with an existing model for atmospheric pressure work. The implications for these measurements and their importance to the turbulent kinetic energy budget are discussed.

SIGNIFICANCE STATEMENT: Surface waves grow through a pattern of atmospheric pressure that travels with the water wave, acting as a pump against the water surface. The pressure pumping, sometimes called pressure work, or the piston pressure, results in a transfer of kinetic energy from the air to the water that makes waves grow larger. To conserve energy, it is thought that the pressure work on the surface must extract energy from the mean wind profile or wind turbulence that sets the shape of the wind speed with height. In this paper, we present direct measurements of pressure work in the atmosphere above surface waves. We show that the energy extracted by atmospheric pressure work fits existing models for how waves grow and a simple model for how waves reduce energy in the turbulent kinetic energy budget. To our knowledge, these are the first reported field measurements of wave-coherent pressure work.

KEYWORDS: Wind waves; Atmosphere-ocean interaction; Boundary layer; Marine boundary layer; In situ atmospheric observations

1. Introduction

a. Background and motivations

The problem of airflow over surface gravity waves is old, with an ongoing record of publications on the topic that started nearly 100 years ago (Jeffreys 1925, 1926; Miles 1957; Phillips 1957; Janssen 1991; Belcher and Hunt 1993; Hristov et al. 2003; Janssen and Bidlot 2023). A nuanced understanding of both the growth of waves and the statistics of atmospheric velocity and pressure over a wavy sea surface is continuing to evolve (Ayet and Chapron 2022). A common central theme in wind-over-wave theories is the relative phase of atmospheric pressure and the sea surface. Under assumptions of potential flow, the pressure is 180° out of phase with the sea surface resulting in no net energy flux or wave growth [see Young (1999), section 4.3.1.1., for a derivation]. For waves to grow through a pressure-driven process, the phase of the atmospheric pressure must be shifted downwind of the wave crest such that there is a low pressure anomaly aligned with upward wave orbital motions (leeward side), resulting in net negative pressure work on the surface. As described in Janssen (1999), this pressure–velocity correlation is expected to persist in the atmosphere above the air–water interface and serves as a sink of kinetic energy in the atmospheric turbulence budget. In this way, the wave-coherent pressure work is an important link between the wave-incoherent turbulent motions that otherwise would be expected to follow boundary layer theory (e.g., Edson and Fairall 1998) and the wave-coherent motions that lead to wave growth.

b. TKE budget in the wave-affected atmospheric boundary layer

Following many previous studies [Janssen (1999), Eq. (8) therein; Cifuentes-Lorenzen et al. (2018), Eqs. (2) and (3) therein; Ayet and Chapron (2022), Eq. (22) therein], the turbulent kinetic energy (TKE) equation in the atmosphere above growing surface waves can be posed as

Denotes content that is immediately available upon publication as open access.

Corresponding author: Seth F. Zippel, seth.zippel@oregonstate.edu

DOI: 10.1175/JPO-D-23-0097.1

$$\tau_{\text{tot}} \frac{d\langle u\rangle}{dz} + \frac{d}{dz}\Pi_w - \rho_a \epsilon = 0, \tag{1}$$

where we have assumed neutral stability and that the turbulent (wave-incoherent) pressure and energy transport terms cancel. Here, $\tau_{\text{tot}} = -\rho_a\langle u'w'\rangle$ is total (turbulent plus wave-coherent) stress, Π_w is the wave-induced KE transport, ϵ is the TKE dissipation rate, $\langle\cdot\rangle$ represents a time average, $u' = u - \langle u\rangle$ is the fluctuating horizontal velocity, and w' is the fluctuating vertical velocity. Fluctuations can be decomposed into the into wave-coherent and wave-incoherent (i.e., turbulent) parts such that $w' = \tilde{w} + w'_t$. The wave-induced KE transport, $\Pi_w = -\langle\tilde{p}\tilde{w} + \rho_a\tilde{u}\tilde{u}\tilde{w}\rangle$, is comprised of the pressure work $\langle\tilde{p}\tilde{w}\rangle$ and a triple velocity product.[1] Janssen (1999) argued that the triple velocity product is expected to be small, and proposed a form for the magnitude and vertical profile of the wave-induced pressure work as

$$\langle\tilde{p}\tilde{w}\rangle = \left\langle p_0 \frac{d\eta}{dt}\right\rangle e^{-2kz}, \tag{2}$$

where k is the wavenumber of surface waves, z is the height above water, and $\langle p_0(d\eta/dt)\rangle$ is the surface pressure work, which can be recognized as the source term for surface wave growth (i.e., the energy flux into surface waves at the surface). Here, Janssen (1999) declares that the e^{-2kz} vertical decay rate comes from the assumption of potential flow.[2] We note that this assumption of vertical form has been disputed, particularly very close to the sea surface. A discussion in Donelan et al. (2006) compares the exponential decay for the pressure (not the pressure work) with the output of the model of Kudryavtsev et al. (2001), finding significant differences very close to the surface. Recognizing these limitations, we continue to follow Janssen (1999) and the suggested vertical decay scale therein, where the wave-induced KE transport gradient becomes

$$\frac{d}{dz}\Pi_w \approx -\frac{d}{dz}\langle\tilde{p}\tilde{w}\rangle = -\frac{d}{dz}\int\left\langle p_0\frac{d\eta}{dt}\right\rangle e^{-2kz}\,dk. \tag{3}$$

The energy input from the wind to waves can be estimated from parameterizations of wave growth used in common wind-wave models,

$$\frac{d}{dz}\Pi_w \approx -\frac{d}{dz}\int\int S_{\text{in}}(f,\theta)e^{-2kz}\,d\theta\,df, \tag{4}$$

where $S_{\text{in}}(f, \theta)$ is the spectral energy input to the surface waves, f is the frequency, θ is the relative wind-wave direction, and k is assumed to follow the linear dispersion relation.

c. Wind-wave input and wave growth rates

Wind-wave growth is commonly parameterized using a growth rate β and the surface wave energy spectrum $E(f, \theta)$,

$$S_{\text{in}}(f,\theta) = \beta(f,\theta)E(f,\theta), \tag{5}$$

with $E(f, \theta) = (1/2)\rho_w g G_{\eta\eta}(f, \theta)$, where ρ_w is the water density and $G_{\eta\eta}(f, \theta)$ is the wave elevation spectrum. Plant (1982) fit numerous existing wave growth datasets, finding a growth rate of

$$\beta(f,\theta) = (0.04 \pm 0.02)\frac{u_*^2}{c^2}\,\omega\cos(\theta), \tag{6}$$

where u_* is the atmospheric friction velocity, $\omega = 2\pi f$ is the radial frequency, and $c = \omega/k$ is the frequency-dependent wave phase speed. Janssen (1989, 1991) showed that the drag over the water depends on sea state, which in turn modifies the growth rate. The new proposed growth rate was

$$\beta(f,\theta) = B\,\frac{\rho_a}{\rho_w}\,\frac{u_*^2}{c^2}\,\omega\cos^2(\theta), \tag{7}$$

where B is the so-called Miles' constant which is a function of the nondimensional critical height, and fraction of wave to total stress $\tilde{\tau}/\tau_{\text{tot}}$. Computation of B is often achieved through iteration as described in Komen et al. (1996) and outlined here in appendix A. In practice, Eq. (7) only deviates from the Plant (1982) formulation at high and low wave age. While the energy input of the very short wind-waves is important for wave growth in community wave models, the contribution of the short waves to the pressure work via Eq. (3) is small due to the rapid decay with height.

Janssen (1999) showed that when winds are large (on the order of 15 m s^{-1}), the wave-coherent pressure work is expected to account for roughly 10%–20% of the local TKE budget (e.g., scaled to $u_*^3/\kappa z$) through Eq. (1). An important implication of Janssen (1999) was to warn of bias in the inertial dissipation method for estimating wind stress (Edson et al. 1991; Yelland et al. 1994), particularly at high wind speeds. However, the energy balance posed through Eqs. (1) and (4) is important for understanding how the wind-wave growth feeds back to atmospheric turbulence, which can modify turbulent statistics and the mean wind profile from classic rigid boundary layer results. As discussed in Ayet and Chapron (2022), the choice of turbulent closure schemes in two-equation turbulence models for airflow over wind waves results in different profiles for ϵ and $\langle u\rangle$ (Ayet and Chapron 2022, Fig. 5 therein).

While there are many existing field measurements of stress, mean winds, and TKE dissipation rate over the open ocean, and some measurements of wave-coherent pressure, there are (to the authors' knowledge) no reported field measurements of wave-coherent pressure work which serves as the mechanistic

[1] We note there is some difference in how the triple velocity product is treated in previous work. Since the focus of this work is the pressure term, not the triple velocity product, we opt for the definition used in Ayet and Chapron (2022) and note the differences here.

[2] The statement in Janssen (1999) that potential flow leads to a decay scale of e^{-2kz} has been disputed by a reviewer of this manuscript. The reviewer argues that a constant wind speed profile is also needed to arrive at vertical decay of e^{-2kz}, and that solutions to the Rayleigh and Taylor–Goldstein equations that impose a logarithmic wind profile result in different vertical decays. In this work, we recognize the e^{-2kz} decay is an imperfect approximation, the validity of which will be tested against field data.

link between the downward flux of energy that makes waves grow, and the loss of energy from atmospheric turbulence.

d. Wave-coherent pressure and velocity: Similarity functions and phase

The wave-coherent pressure work depends on the magnitude and difference in phase between the wave-coherent pressure and the wave-coherent vertical velocity. In brief, the real part of the wave-coherent cross-spectrum of p and w, $\mathrm{Re}\{G_{\tilde{p}\tilde{w}}(f)\}$, can be estimated using the power spectrum of sea surface elevations $G_{\eta\eta}(f)$, and the cross-spectra and phase of p and w with the sea surface, respectively:

$$\mathrm{Re}\{G_{\tilde{p}\tilde{w}}(f)\} = \frac{|G_{\eta p}||G_{\eta w}|}{G_{\eta\eta}} \cos(\Phi_{\eta p} - \Phi_{\eta w}). \tag{8}$$

where $G_{\eta p}$ is the cross-spectrum of surface wave elevation and atmospheric pressure, $G_{\eta w}$ is the cross-spectrum of sea surface elevations and vertical velocity, and Φ is the spectral phase. More on Eq. (8) can be found in appendix B. Therefore, a model for $|G_{\eta p}|$, $\Phi_{\eta p}$, $|G_{\eta w}|$, and $\Phi_{\eta w}$ would similarly predict the magnitude and vertical shape of wave-coherent pressure work, and be relevant to the atmospheric TKE equation.

Previous studies have separately reported wave-coherent pressure (Hare et al. 1997), and wave-coherent velocities (Hare et al. 1997; Grare et al. 2018) in terms of similarity functions. Both of these studies sought nondimensional forms for wave-coherent parameters, and posed them as functions of nondimensional height kz, spectral inverse wave age $U(z)/c$, and nondimensional atmospheric forcing u_*/c. Hare et al. (1997) suggested the wave-coherent pressure should be normalized as

$$|N_{\eta p}| = \frac{|G_{\eta p}|}{\rho_a G_{\eta\eta} k c^2} = \frac{|G_{\eta p}|}{\rho_a g G_{\eta\eta} \tanh(kd)}. \tag{9}$$

Hare et al. (1997) found agreement at strong winds for the real part of the pressure similarity function and the potential flow solution, $N_{\eta p} = (U/c - 1)^2 \exp(-kz)$.

Hare et al. (1997) also scaled the wave-coherent vertical velocity as

$$|N_{\eta w}| = \frac{|G_{\eta w}|}{\omega G_{\eta\eta}}. \tag{10}$$

This form is convenient since $N_{\eta w}$ should approach 1 at the surface to be consistent with the no-slip boundary condition.

Both Hare et al. (1997) and Grare et al. (2018) found the vertical velocity similarity function decayed exponentially as $\exp(-\alpha kz)$, where $\alpha = 1$ is the decay scale from potential flow theory. However, fits to the data by Grare et al. (2018) suggest decay rates less than unity, with best fit α in the range 0.62–0.82. Grare et al. (2018) reported correlation coefficients with four different forms for $N_{\eta w}$ as functions of $U(z)/c$ and kz, finding highest correlation with a four parameter fit. The phase between sea surface elevation and vertical wind velocity $\Phi_{\eta w}$ has been shown to exhibit a sharp transition across the critical layer, or the height at which the wave speed and wind speed match, $\langle u(z)\rangle = c$ (Hristov et al. 2003; Grare et al. 2013a, 2018). This is often shown as a spectral critical layer in deep water, $f_c = g/(2\pi\langle u\rangle)$, which allows for comparing the local wind speed to the measured spectral phase. Hristov et al. (2003) and Grare et al. (2013a, 2018) showed phase shifts between 90° and 180° across the critical layer frequency in different field measurements made from R/P *FLIP*. These phase shifts have been used as support for the critical layer mechanism (sometimes called the matched layer mechanism) for wind-wave growth. Hristov et al. (2003) solved the Rayleigh equation numerically to compare against measured $\Phi_{\eta w}$, finding constant values on either side of the critical layer which agreed well with their measurements.

The phase between the sea surface elevation and atmospheric pressure remains a topic of much interest, as it directly links to the growth rate of wind waves. Field and laboratory experiments (Snyder et al. 1981; Hare et al. 1997; Donelan et al. 2005; Grare 2009; Grare et al. 2013b) have sought to measure the pressure–sea surface phase from both static, and wave-following platforms finding wave-coherent pressure phases between $\Phi_{\eta p} = 120°$ and $\Phi_{\eta p} = 180°$. However, the phase of pressure at the wavy sea surface remains of considerable interest. For example, the recent two-phase DNS study of Wu et al. (2022) reports much larger phase shifts than have been measured in the field (on the order of 90°), and suggested the importance of mechanisms related to wave steepness as well as wave age.

e. Structure of this work

Here, we focus on the magnitude and spectral shape of wave-coherent atmospheric pressure work, motivated by its relevance to the turbulent kinetic energy (TKE) budget of the atmospheric boundary layer. To do this, we will use measurements from a fixed Eulerian reference frame which offers many logistical advantages. While recognizing that these fixed-frame measurements cannot capture important statistics below the wave crests which may deviate from their above-crest statistics (Grare et al. 2013b), they can still be used to evaluate the pressure work relevant to the Eulerian TKE equation in the atmosphere.

Section 2 describes the field site, the data collection, and the data processing. Section 3 presents the results, including measured phase and magnitude of wave-coherent pressure and velocity, and the resulting estimates of pressure work. These measurements are compared against the similarity functions and decay scales suggested from previous studies, and to the Janssen (1999) model for pressure work. Section 4 discusses the implications of these measurements for the atmospheric wave-affected boundary layer, and avenues for future work on the topic. A summary is presented in section 5.

2. Methods

a. Site description and measurement overview

Measurements were made from an open-lattice steel tower (Fig. 1) deployed in roughly 13-m water depth in Buzzards Bay, Massachusetts. Buzzards Bay is a 48 km × 12 km basin open on the southwest side to Rhode Island Sound. The

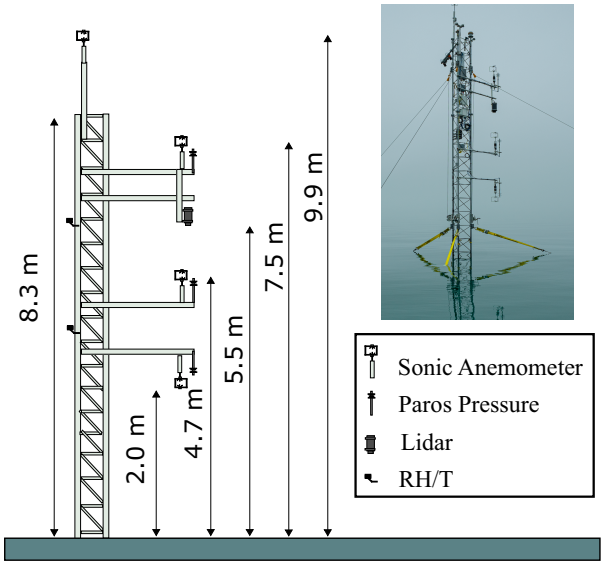

FIG. 1. A schematic showing a subset of the air-side instrumentation used in this study, shown with a photograph of the tower (courtesy of S. Whelan). Heights are referenced to the tower but represent the approximate distance to mean water level over the two-month deployment. Each boom held instruments 1.2 m from the nearest tower vertical strut.

average depth is 11 m, with a tide range of 1–1.5 m, depending on the neap–spring cycles. Winds in Buzzards Bay are commonly aligned with the long axis of the bay (from the northeast or southwest), and are often strong in the fall and winter. The tower was deployed near the center of the bay at 41.577 638°N, 70.745 555°W for a spring deployment lasting from 12 April 2022 to 13 June 2022. Wind speeds were measured up to 16 m s^{-1}, and were large and sustained during a 3-day event in early May that will receive additional focus here (Fig. 2).

Atmospheric measurements included three primary instrument booms that housed paired sonic anemometers (RM Young 81000RE) and high-resolution pressure sensors (Paros Scientific). The pressure sensor intakes were terminated with static pressure heads (Nishiyama and Bedard 1991), which reduce the stagnation pressure contribution to the measured pressure. The tower booms were aligned at 280° such that the northeast and southwest winds would be unobstructed by the tower's main body. A fourth sonic anemometer (Gill R3) was extended above the tower such that it was open to all wind directions and clear of wake by the tower structure. A single point lidar (Riegl LD90-3i) was mounted to the highest boom and measured the water surface elevation underneath the anemometer and pressure sensors to within a few centimeters horizontally. All instruments were time synchronized with a custom "miniNode" flux logger that aggregated the data streams from each instrument. The miniNode is an in-house constructed datalogger used to time synchronize multiple serial data streams, to control power (duty cycle) instruments, and to communicate with a shoreside user. It is composed of a BeagleBone computer with several custom-made data/power boards and is housed in a water-tight Delrin cylinder equipped with Subconn bulkhead connectors to connect to instrumentation. The version used in this study updates similar miniNode dataloggers used in Coupled Boundary Layer Air–Sea Transfer (CBLAST; among many other previous studies) which

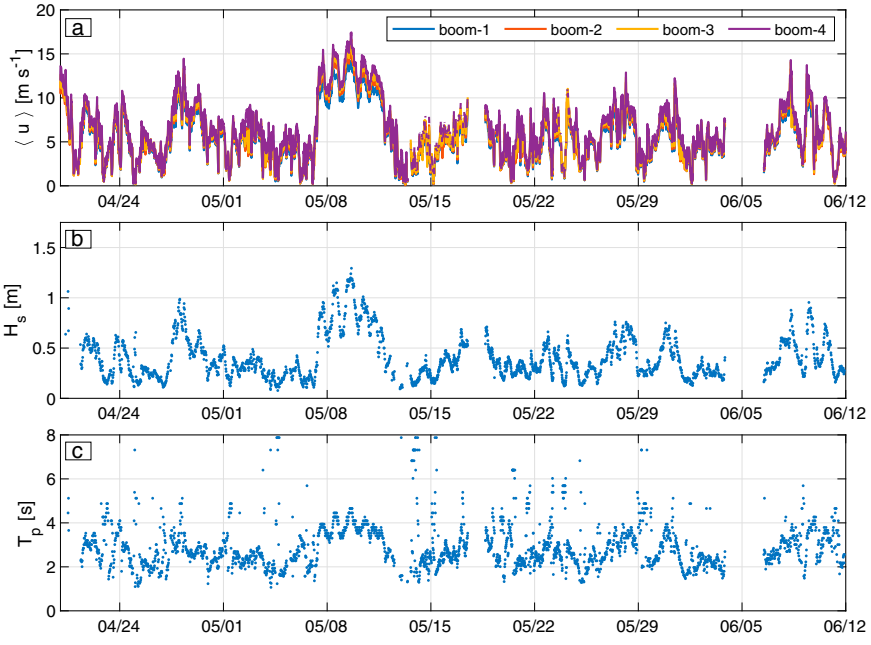

FIG. 2. (a) 20-min mean windspeeds measured from the four vertical levels. Here, boom-1 represents the lowest level boom shown in Fig. 1. (b) Significant wave heights and (c) peak wave periods from BBASIT are shown above.

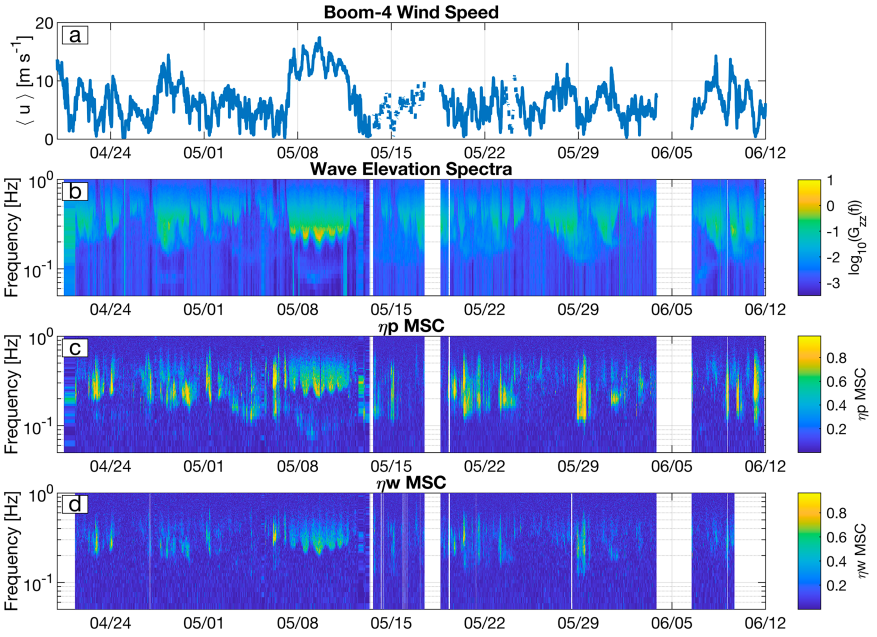

FIG. 3. (a) Boom-4 wind speed. (b) Wave elevation spectra. (c) Magnitude squared coherence between the sea surface and atmospheric pressure from boom-1. (d) Magnitude squared coherence between the sea surface and atmospheric vertical velocity from boom-1.

required synchronization of data streams from multiple different sensors (Edson et al. 2007). The heights of each instrument above the deployment mean water level are shown alongside a photograph of the tower in Fig. 1. Additional atmospheric and wave measurements on the tower included shortwave and longwave radiometers (Kipp and Zonen) a stereo camera pair (IOI 5MP Victorem), two RH/T sensors (Vaisala), and a standard lower-resolution barometer (Setra).

Subsurface velocity and pressure measurements were made with an array of six Nortek acoustic Doppler velocimeters (ADVs) paired with high-resolution Keller pressure sensors sampling at 32 Hz. These measurements were primarily used in this study for assessing surface wave directions. Additional water-side measurements were made (including temperature, conductivity, currents, turbulence, acoustic backscatter, and more), which will be described in a subsequent manuscript, and will not be used in the analysis here.

The sonic anemometers and pressure sensors were sampled continuously, with sampling frequencies of 20 Hz (Gill R3), 32 Hz (RM Young, booms 1–3), and 16 Hz (Paros pressure). The lidar was nominally sampled at 20 Hz and sampled for 40 min starting at the top of each hour. Data were recorded in 20-min-long files, and time averages and spectra are estimated over these 20-min segments. Timing was synchronized such that the start and end of each instrument's 20-min files were aligned to less than 10 ms. There is some additional unknown timing delay between instrument sampling and instrument data output that depends on the manufacturer specifications which are not always published. As an example, the Gill R3-50 manual reports that sampling the three pairs of transducers in sequence over 7 ms with a 3-ms delay before sending data. We estimate the resulting time alignment between instruments as being roughly one instrument sample (50 ms) to account for variable instrument delays and timing variance from the datalogger. For waves with frequencies of 0.1, 0.2, 0.4, and 0.8 Hz, a 50-ms timing offset would result in 1.8°, 3.6°, 7.2°, and 14.4° error in phase, respectively. Therefore, more variance is expected in higher-frequency estimates of spectral phase due to the sub-ping timing alignment uncertainty.

b. *Spectral and cross-spectral analysis*

Instruments were linearly interpolated to a 20-Hz time grid for spectral and cospectral processing. Power spectra and cross-spectra were estimated using the overlapping-segmented averaging method as implemented by MATLAB's "pwelch" and "cpsd" functions. Each time series was linearly detrended and processed with 2048-sample windows (1.69 min) tapered with a Hamming window with 50% overlap between segments. The interpolation resulted in some high-frequency deviation from spectra made from the original (not interpolated) time series, although this was confined to frequencies larger than 1 Hz, above the wave band frequencies of interest to this study. For example, interpolated sonic anemometer spectra were observed to be roughly 10%–20% lower than noninterpolated spectra at 5 Hz, with no noticeable deviation at 1 Hz. Confidence intervals for power spectra follow the standard χ^2 form, with normalized errors estimated as $\chi^2_{\mathrm{DOF}}/\mathrm{DOF}$, where DOF is the number of degrees of freedom. For the 20-min data segments here, power spectra would have errors of roughly 50% of the measured spectral estimator. Cross-spectral and phase variances depend both on the DOF, and on the magnitude

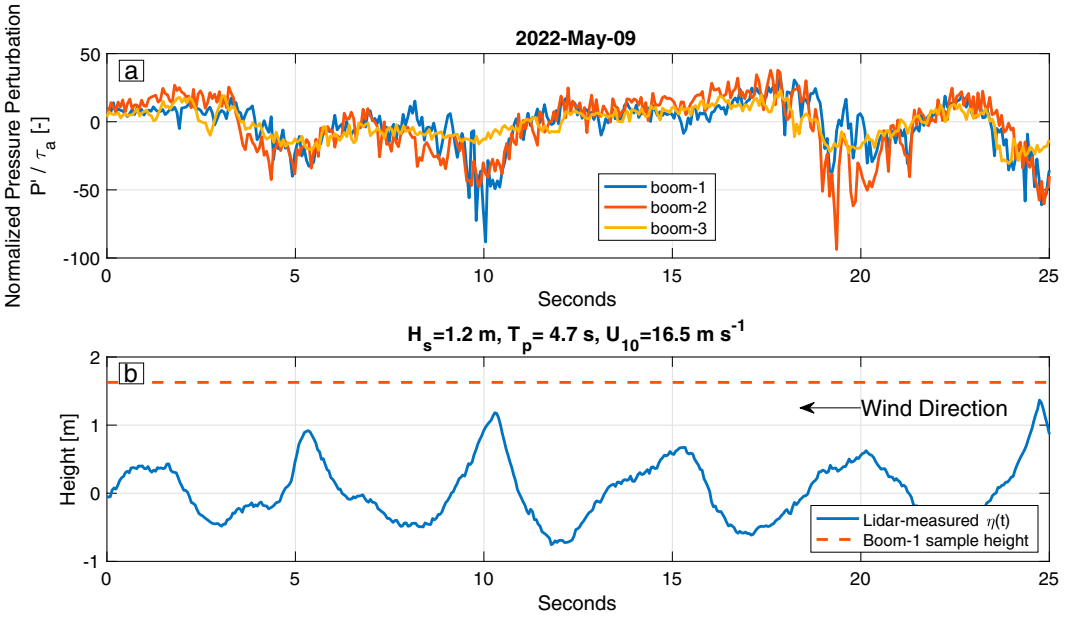

FIG. 4. (a) A time series of normalized pressure perturbations measured from the three Paros pressure sensors. (b) A time series of sea surface elevation measured by the single point lidar (solid blue) and the boom-1 wind and pressure sample height (dashed orange) that is closest to the water surface. Heights in (b) are referenced to the 20-min mean water level; boom-1 is closer to the surface here than referenced in Fig. 1 due to the combined tidal stage and wind-driven setup. Pressure in (a) is normalized by the wind stress, estimated using a 20-min averaging window. The pressure perturbation is the deviation from a 30-s moving average filter. Large negative atmospheric-pressure perturbations are aligned with the passage of wave crests. Waves and wind can be imagined as moving right to left in the time series, such that lidar measures the leeward (downwind) face of the wave first.

squared coherence (MSC) between the two signals. The error formulas are presented in Bendat and Piersol [2011, Table 9.1 and Eq. (9.52) therein]. For MSC of 0.2, 0.3, and 0.4, the expected standard deviation in phase for a given 20-min cross-spectrum recorded at 20 Hz are 25.05°, 19.78°, and 16.48°, respectively. For context, averaging eight 20-min cross-spectral estimates reduces the expected standard deviation in phase to 8.85°, 7.0°, and 5.83°, respectively.

Separation of the pressure work cospectrum into wave-coherent and wave-incoherent terms for the atmospheric measurements was done following Eq. (8), which is described in more detail in appendix B. This separation between wave-coherent and wave-incoherent components generally follows from previous studies and textbooks (e.g., Bendat and Piersol 2011; Veron et al. 2008; Grare et al. 2013b). The total wave-coherent pressure work at a measurement height can be found by integrating Eq. (8) in frequency, $\langle \tilde{p}\tilde{w} \rangle = \int \mathrm{Re}\{G_{\tilde{p}\tilde{w}}(f)\} df$, with the integral evaluated in the wave band (between 0.1 Hz $< f <$ 1 Hz). Although this is somewhat arbitrary, it was found that decreasing the low-frequency limit added noise in the integrated pw estimates. Increasing the high-frequency limit resulted in minor changes but was set to where there were minimal differences between interpolated and noninterpolated spectra. Visual inspection of the MSC (Fig. 3) shows the most coherence at frequencies 0.2 Hz $< f <$ 0.8 Hz, well inside the chosen integration bounds.

c. *Estimation of S_{in} and β, and Janssen's (1999) pressure work*

Wind-wave input S_{in} was estimated using the measured energy spectrum $E(f)$, and the measured wind friction velocity u_* following Eq. (7) for computation of β using the procedure described in Komen et al. (1996). Wave directions were measured using velocity and pressure measurements from an acoustic Doppler velocimeter (ADV) roughly 2 m below the water surface (Herbers et al. 2012; Thomson et al. 2018). Wavenumber $k(f)$ was estimated using the finite-depth linear dispersion relation, $(2\pi f)^2 = gk \tanh(kd)$, where d is the local water depth, and g is the acceleration due to gravity. Due to the relatively short fetch-limited waves measured at this location, most wave frequencies were unaffected by water depth via the dispersion relation. For example, at 0.2 Hz, the finite-depth wavelength is 97% of its deep-water equivalent. Surface currents were typically less than 20 cm s^{-1}, and dispersion corrections were not considered since they are relatively small for waves at frequency $f < 1$ Hz.

Combining the Janssen (1999) form of atmospheric pressure work [Eq. (2)] with parameterizations for the surface wave energy flux gives a model for $G_{\tilde{p}\tilde{w}}(z, f)$ that depends on the wave energy spectrum and the wind stress (via the parameterized growth rate), and the relative wind-wave direction. The spectral pressure work can be estimated as

$$G_{\tilde{p}\tilde{w},\mathrm{model}}(z, f) = \rho_a \beta(f) E(f) e^{-2k(f)z}, \tag{11}$$

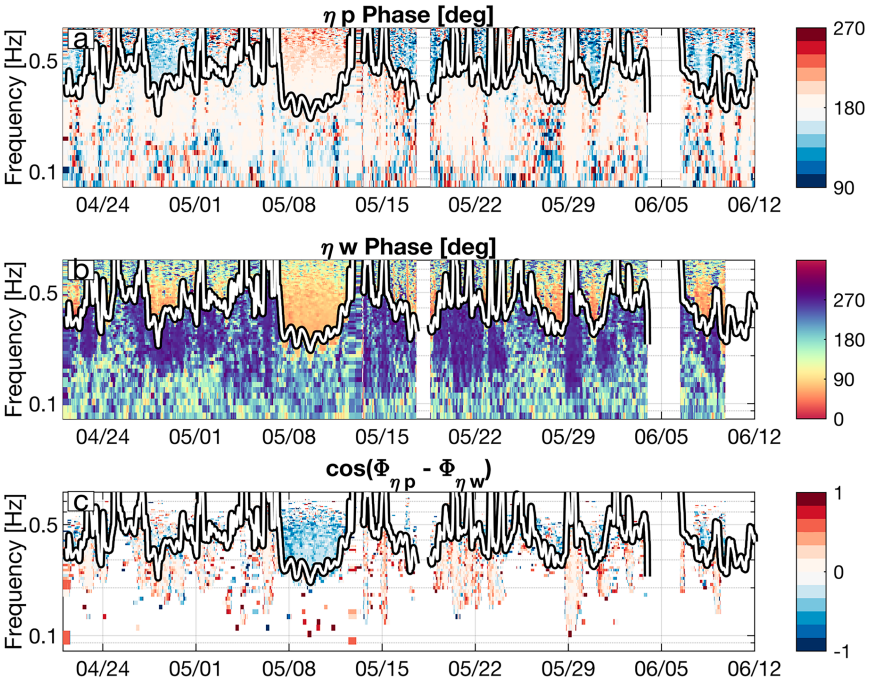

FIG. 5. Phases of (a) pressure and (b) vertical velocity with respect to sea surface elevation, with (c) the cosine of their difference. The color axis for (a) is zoomed to better see slight differences near 180° of phase, and the color axis of (c) is chosen such that blues align with a downward flux [see Eq. (8)]. The bounded white lines in (a)–(c) show $\max\{f_p, f_c\}$, where f_p is the peak frequency and $f_c = g(2\pi\langle u\rangle)^{-1}$ is frequency of the critical layer in deep water. Estimates in (c) with associated magnitude squared coherence less than 0.1 are excluded. Data have been smoothed using a 4-h moving average filter for visibility.

where we have assumed winds and waves are aligned, and that either the Plant (1982) or the Janssen (1991) growth rate β is used. The total wave-coherent pressure work can be estimated by integrating the above equation in frequency.

3. Results

a. *Wave coherent pressure and velocity*

Atmospheric pressure and velocity were found to be coherent with the waves, particularly during strong winds. Figure 3 shows a time series of the wave elevation spectrum along with the MSC of ηp and ηw. The strongest coherence for p and w occurs during the 3-day high-wind event on 8–10 May. Periods of high pressure coherence also align with decaying waves; however, these periods often have weaker coherence in velocity, whereas high-wind events are associated with high coherence in both p and w.

During high-wind events, the atmospheric pressure was found to be shifted from the potential flow 180° phase with the sea surface elevations, consistent with wind-wave growth theories (Miles 1957; Janssen 1991) and past measurements of wave-coherent pressure (Snyder et al. 1981; Hare et al. 1997; Donelan et al. 2005). During these events, low atmospheric pressure perturbations were seen slightly downwind of wave crests, and high atmospheric pressure perturbations were measured over wave troughs. An example is shown in Fig. 4, during a high-wind event that took place in early May where the lowest boomed instruments were particularly close to the wave crests (for the shown example, the middle of the instrument sampling volume was just under 30 cm above the highest wave crests). Wave-induced pressure perturbations are visible from all three booms with pressure perturbations as large as $p' \sim 50$–$100\tau_a$ over the wave crests. Pressure perturbations were generally larger at the booms closer to the surface. Although the boom-2 pressure shown in Fig. 4 occasionally exceeds the boom-1 pressure, on average the perturbations were measured to decrease with height. Perturbations were not seen over every wave crest/trough, but were seen sporadically over groups of 5–10 sequential wave crests, particularly during high-wind events.

A time series showing the spectral phase of pressure and vertical velocity for the full deployment is shown in Fig. 5. Both the pressure and the vertical velocity phase (Figs. 5a,b) exhibit a phase transition across a frequency defined as $f_{\max} = \max\{f_p, f_c\}$, where f_p is the peak wave frequency and f_c is the deep-water critical layer frequency [the frequency where $U(z) = c$]. Recognizing that relative wind and wave directions can result in modified or multiple critical layers, we opt for the unidirectional deep-water critical layer frequency for its simple representation. Pressure phases shift from $\Phi_{\eta p} \sim 180°$ near $f_{\max}$ to $\Phi_{\eta p} < 180°$ for frequencies higher than $f_{\max}$. This phase shift holds for frequencies just above

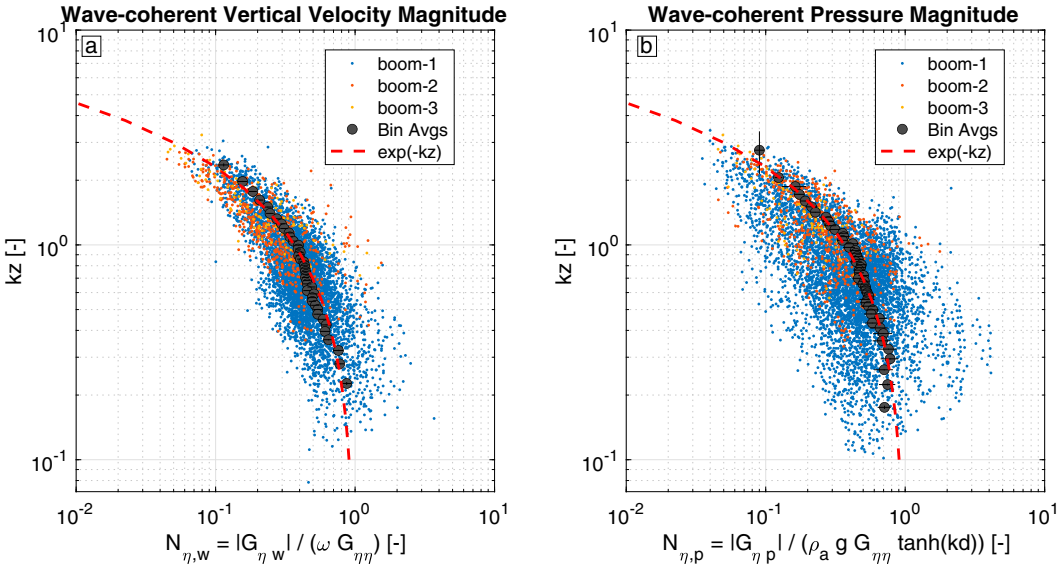

FIG. 6. Spectral similarity functions for wave-coherent (a) vertical velocity and (b) pressure plotted against vertical scale kz. Small colored dots show 20-min spectral data for booms-1–3 (mean boom elevations shown in Fig. 1). Estimates with low MSC have been excluded. Bin averages are made by averaging 125 sequential descending points in kz, and are shown with 95% confidence intervals defined as twice the standard error. Bin averages agree well with the $\exp(-kz)$ decay rate shown by the dashed red line over $0.2 < kz < 3$.

$f_{\max}$ during the high winds in May, which ranged between $165° < \Phi_{\eta p} < 180°$, despite the visually apparent red coloring at high frequency in Fig. 5a. The high-frequency shift to $\Phi_{\eta p} > 180°$ during this event is discussed further in appendix C, and is believed to be an effective phase bias due to a horizontal offset that primarily impacts high frequencies, and not the phase difference $\Phi_{\eta p} - \Phi_{\eta w}$.

Similar to previous work, vertical velocity phases consistently shift from $\Phi_{\eta w} \sim 90°$ at frequencies above $f_{\max}$, to $\Phi_{\eta w} \sim 270°$ below $f_{\max}$. Since both pressure and vertical velocity phases shift similarly, the difference in frequency $\Phi_{\eta p} - \Phi_{\eta w}$ varies more weakly with frequency than pressure or vertical velocity phase alone. Still, there is an important change in sign of $\cos(\Phi_{\eta p} - \Phi_{\eta w})$ that occurs across $f_{\max}$, with negative values (blue in Fig. 5c) for frequencies above $f_{\max}$ and generally positive values (red in Fig. 5c) for frequencies below $f_{\max}$. This change in sign reflects the phase difference that is consistently equal to $\Phi_{\eta p} - \Phi_{\eta w} \approx 110°$ for $f > f_{\max}$. It is this small phase shift that deviates roughly 20° from quadrature that allows for the downward (negative) wave-coherent pressure work fluxes.

b. *Similarity functions and decay scales*

Wave-coherent vertical velocity and pressure are consistent with a vertical decay of the form $\exp(-\alpha kz)$, and are consistent with the decay rate $\alpha = 1$ suggested by potential flow solutions (Young 1999). Figure 6 shows measurements scaled as suggested by the Hare et al. (1997) similarity functions. Both $N_{\eta w}$ and $N_{\eta p}$ approach 1 at small kz, and binned values from all three booms are in close agreement with $\exp(-kz)$. Although only measurements from boom-1 extend below roughly $kz = 0.5$, data from all three booms agree for $kz > 0.5$. These measurements are within the range of decay rates found in previous studies $\alpha_w = 0.63$ (Grare et al. 2018) and $1 < \alpha_p < 1.8$ (Donelan et al. 2006). However, the decay rates from this study appear much closer to the potential flow solution on average (i.e., $\alpha = 1$).

c. *Wave-coherent pressure work*

Combining measurements of the wave-coherent pressure and vertical velocity allow for estimation of the wave-coherent pressure work through Eq. (8). These estimates can be compared against the directly measured cospectra of velocity and pressure, which include both wave-coherent and wave-incoherent information (Fig. 7a). Cospectra of pressure work show clear negative pw in the wave band, counter to the background wave-incoherent fluctuations which are positive (Fig. 7a). Both p and w show strong coherence with waves, η, in the wind wave frequency band ($0.05 \text{ Hz} < f < 1$ Hz, Fig. 7b), suggesting the negative pw is due to surface waves. A wave-turbulence decomposition (described in appendix B) shows that the pw cospectrum is similar in magnitude and shape to the Janssen (1999) model [Eq. (11)]. The spectral decay term, $\exp(-2kz)$ is essential in this fit, and is consistent with the decays measured in Fig. 6. Still, Eq. (11) over predicts pw at roughly $f < 0.25$ Hz and under predicts pw for roughly $f > 0.35$ Hz, suggesting some possible deficiencies in the modeled vertical decay and/or growth rate related to frequency.

d. *Downward pressure work fluxes during high winds*

The time series of the frequency-integrated wave-coherent pw cospectrum (hereafter called measured pressure work) is consistent with the Janssen (1999) model at the lowest boomed

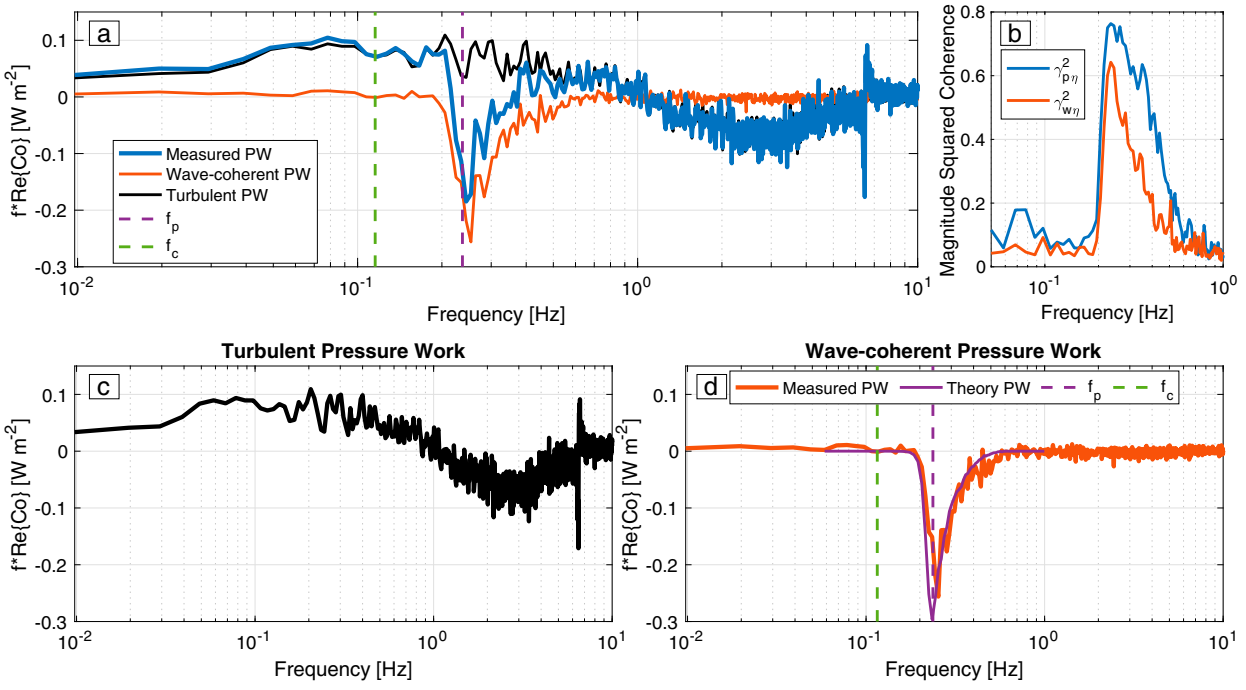

FIG. 7. (a) Six 20-min *pw* cospectra from 9 May 2022 are averaged (blue) and shown alongside the decomposed turbulent [black, also shown in (c)] and wave-coherent [orange, also shown in (d)] components. (b) The magnitude squared coherence γ^2 between η and p, as well as between η and w are shown. There is strong coherence for pressure and vertical velocity in the wave band ($0.1 < f < 1$ Hz), which allows the (c),(d) decompositions. The Janssen (1999) model for atmospheric *pw* is shown in purple in (d) [Eq. (11)], which aligns well in both magnitude and shape to the measured cospectrum.

level over the entire high-wind event, which lasted roughly 7–11 May 2022. Figure 8 shows the measured pressure work against the energy fluxes estimated from the Janssen (1999) model. There is good agreement in both magnitude and shape between the measurements and model, with the model slightly overpredicting energy fluxes. These results are fairly consistent if the wave growth rate β is taken from either Plant (1982) or Janssen (1991). Moderate agreement was seen at booms 2 and 3 (not shown), at the expected but much lower energy levels (0.06 and 0.02 W m^{-2}, respectively, during the highest winds on 9 May).

e. *Upward pressure work fluxes during relaxing winds*

The measured pressure work fluxes occasionally switch sign, such that there is an upward flux (waves giving energy to the wind). This occurs when the phase difference $\Phi_{\eta p} - \Phi_{\eta w}$ is slightly less than 90°, and is most often observed for decaying waves at frequencies $f < f_{\max}$. Many low-wind events correspond to low MSC, which makes estimation of the upward wave-coherent pressure work more challenging. However, during quickly decreasing winds there is enough remnant wave energy to observe high MSC and upward pressure work. For example, strong pressure-wave coherence and upward (positive) pressure work was observed on 29 May after a rapid decrease in wind speed (as shown in Fig. 9). As the winds drop, the frequency of the spectral critical layer increases. These upward fluxes from the waves are not considered in the Janssen (1999) model which may result in an overestimate of the wave energy sink in the TKE budget.

Previous studies have measured waves driving mean winds in the laboratory (Harris 1966), and shown upward momentum fluxes from swell moving faster than winds (Grachev and Fairall 2001); however, treatment of these wave-to-wind fluxes in both atmospheric boundary layer schemes and community wave models remains poorly constrained by field data. Commonly implemented source terms in community wave models (i.e., the ST4 physics package; Ardhuin et al. 2010) compute swell dissipation rates largely based on the analysis of Ardhuin et al. (2009), which used altimeter data to track swell energy loss along great circles. Although there was not sufficient data from the example shown in Fig. 9 for an extensive analysis of wave-to-wind fluxes, the pressure work method presented here could prove useful for future field studies to refine understanding of processes by which swell loses energy to the atmosphere (Hanley and Belcher 2008).

f. *Overall data/model agreement*

The Janssen (1999) model provides reasonable agreement with the measurements, particularly at high winds. Figure 10 shows a direct comparison for measured and modeled wave-coherent pressure work. For energy fluxes above 3×10^{-2} W m^{-2}, the data and model are in good agreement. For lower wind speeds (below approximately 10–12 m s^{-1}), the data and model are correlated, but with much smaller measured fluxes than predicted by

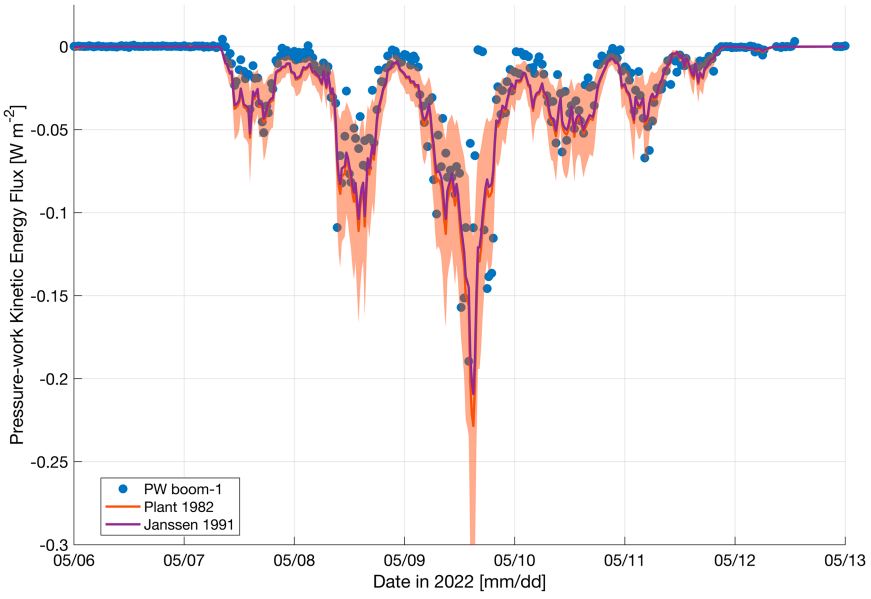

FIG. 8. A comparison of the time series of wave-coherent energy fluxes estimated from measurements made from the lowest-elevation boom (blue) and from the Janssen (1999) model using the Plant (1982) growth rate [orange with shaded error bars, Eq. (6)], and the Janssen (1991) growth rate [purple, Eq. (7)] over the 3-day high-wind event in early May 2022. Error bars are derived from the reported coefficient uncertainty in Plant (1982).

the model. This may be due to the reversal of the direction of the pressure work flux at frequencies lower than the critical layer frequency, which is not considered in the model as it is calculated here. Conversely, there may be fluxes that were not measured well due to low coherence at lower frequencies, as can be seen by the data excluded in Fig. 5c. Although integrated fluxes were still calculated, there may be bias introduced from the frequencies with very low MSC. These tended to skew toward lower frequencies, which often exhibited erroneously large upward fluxes. This was found to be due to the shape of the pressure spectra, which exhibited spectral slopes between f^{-1} and f^{-2} outside of the wave band (i.e., increasing pressure variance at decreasing frequency).

4. Discussion

a. *Prediction of pressure-work fluxes*

While there is compelling consistency between the Janssen (1999) *pw* model and the pressure work measurements during this event, it is perhaps not generalizable without more events. As noted by several authors, there is still considerable spread in existing data for growth rate β, resulting in 50% uncertainty in the coefficient reported by Plant (1982) [as seen in Eq. (6)]. Including this uncertainty would put the majority of measured *pw* within the uncertainty bounds in wind-wave energy flux. The spread in existing growth rate data is somewhat expected. Under the critical layer mechanism, the growth rate is governed by the ratio of wind speed curvature to shear at the critical layer height, $\chi = U''(z_c)/U'(z_c)$. The value of χ is expected to be inherently variable due to the tendency of derivatives to enhance variability. Therefore, small deviations from an expected logarithmic profile (used to inform parameterized growth rates) would cause much larger variability in growth rate (Hristov and Ruiz-Plancarte 2014).

Still, close inspection of Fig. 7d shows the largest difference between the theory and measured wave-coherent pressure work occurs near 0.25 Hz, just before the measured cospectrum falls off toward zero. This effect is fairly consistent across the May high-wind event, suggesting that there may be some deficiencies of the model. However, it is unclear if the mismatch is due to the growth rate, the vertical decay function, the assumption of unidirectional waves, or another unidentified mechanism. The vertical decay function is particularly suspect, as the potential flow exponential decay has been shown to fall short when compared to more detailed numerical models (Kudryavtsev et al. 2001; Donelan et al. 2006).

Several recent studies have also suggested variability in the wave growth rate with wave steepness as well as wave age (e.g., Buckley et al. 2020; Wu et al. 2022). Therefore, it could be that the spectral growth rate decreases near the peak in relation to a roll-off in spectral steepness. Last, this roll-off could be due to unaccounted-for directional spreading effects. Plant (1982) integrated a directional spreading function, which modified the unidirectional growth rate by roughly 20% [Plant 1982, Eqs. (10)–(12) therein]. Finite depth effects that modify the wave phase speed and shape of the wave orbital motions were not expected to be large, since at 5 s (the frequency where wave-coherent pressure work approaches zero in Figs. 7a,d) the finite depth phase speed is still 97% that of the deep water limit.

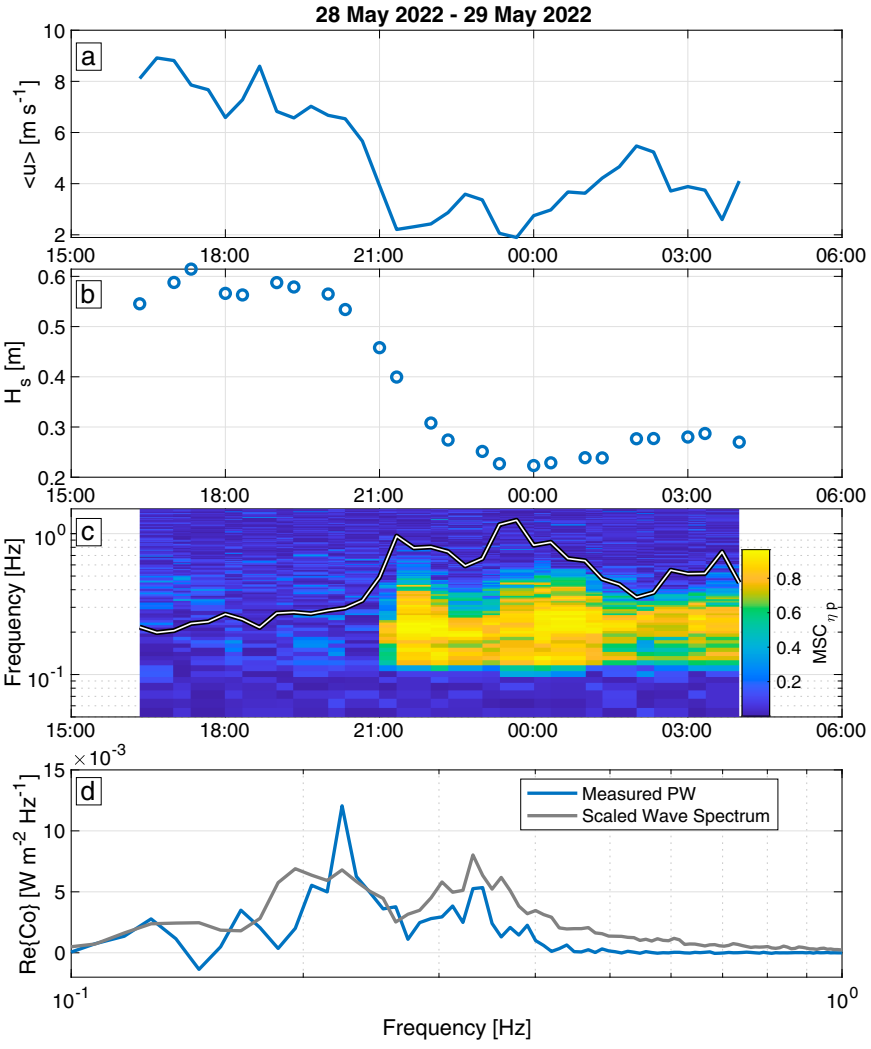

FIG. 9. An example of upward pressure work during a decaying wind-wave event in late May. (a) 20-min mean wind speed measured from boom-4 (height roughly 10 m). (b) Significant wave height. (c) Magnitude squared coherence between the sea surface elevation and boom-1 pressure and the deep-water critical layer frequency (white line). (d) Wave-coherent pressure work spectrum (blue) shown with a scaled wave elevation spectrum (gray) for reference. Spectra in (d) were averaged over the 2-h period from 2100 to 2300 local time for visibility.

As noted in Ayet and Chapron (2022), there is some disagreement over the expected shape of the wave-induced transport term Π_w, which depends heavily on wave-coherent pressure work and which could impact mean wind profiles and turbulent statistics in the atmospheric boundary layer (Fig. 5 therein). Very recent work from Janssen and Bidlot (2023) investigated the feedback between wave-supported energy fluxes and changes to the mean wind profile. Under a Miles critical layer growth mechanism, the curvature of the mean wind profile sets the wave growth rate β. The discussed feedback is that the wave-coherent energy fluxes can modify the shear profile, which would then result in a smaller growth rate. Janssen and Bidlot (2023) found this nonlinear effect was visible but relatively small at $\langle u \rangle \sim 15$ m s^{-1}, with a large reduction of growth rate at $\langle u \rangle = 50$ m s^{-1} (see Fig. 1 therein). Continued work to understand the magnitude and decay rate of $\langle \tilde{p}\tilde{w} \rangle$ and its relation to the mean wind profile, particularly at high winds, will be a fruitful future direction of study.

b. *Flux measurements from low-height sensors at sea*

There is a growing interest in measuring fluxes from autonomous platforms at sea which frequently measure wind speed from a low mean height (e.g., ~1 m for wave gliders). The approach is often to use bulk flux algorithms (Edson et al. 2013) and/or the inertial dissipation method (Edson et al. 1991; Yelland et al. 1994). The extent to which the wave boundary layer influences estimates of surface fluxes, particularly at low measurement heights, has yet to be fully determined. The results here support the arguments from Janssen (1999) that inertial dissipation estimates are likely biased due to a deficit of

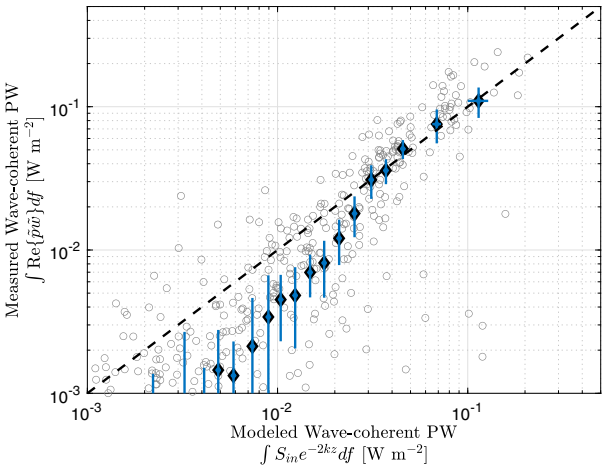

FIG. 10. A scatterplot shows a comparison of the measured and modeled frequency-integrated wave-coherent pressure work above. Data–model agreement is good during high-energy conditions. At lower energy levels, the model does not capture the reversal of sign at the critical frequency and overpredicts the energy draw down from the atmospheric boundary layer. Open gray circles show integrated 20-min cospectral values, and blue diamonds show binned averages with 95% confidence intervals. Bin averages are made by averaging 25 sequential ascending points, and confidence intervals defined as twice the standard error.

dissipation related to the wave growth mechanism. However, we emphasize here that this bias is small at wind speeds less than ~10 m s^{-1}, even for low measurement heights. At moderate wind speeds, the Janssen (1999) model does a reasonable job predicting the pressure work fluxes at wind speeds 10–15 m s^{-1}, suggesting a wave correction could be applied to inertial dissipation estimates of stress. Since wave spectra are commonly measured from autonomous sea-going platforms, these corrections would not pose onerous additional measurement constraints. The reference to specific wind speeds is not intended to be universal, since the data used in this study were in a limited fetch environment and will have a different wave age than similar wind speeds in open ocean conditions.

Whether or not the mean wind speed measured from such platforms exhibits bias due to wave-affected boundary layer influences is also of debate. A discussion in Hristov and Ruiz-Plancarte (2014) suggests that the wind profile wave bias is controlled by the wave age and wave steepness, concluding that at the commonly observed wave steepness the wind profile wave bias is small (order 2%). However, this study did not consider feedbacks between sea state and the roughness length z_0 and used the Charnock coefficient as an experimental parameter. These feedbacks through the roughness length were a central part of the findings of Janssen and Bidlot (2023). The results presented here focus on the energy fluxes and not the mean wind speed profiles. However, given that the pressure work fluxes are small until higher wind speeds, it is unlikely wave-driven fluxes would have a significant impact on mean wind profiles for wind speeds less than 10–12 m s^{-1}. For storm and high-wind conditions (above roughly 12–15 m s^{-1}), the wave-driven pressure work fluxes become a larger fraction of the TKE equation and the impact to Monin–Obukhov (MO) similarity functions central to bulk flux formulas (Edson et al. 2013) has yet to be determined. More work will be needed to justify the use of bulk formulas from these low-level wave-following platforms at high wind speed.

5. Conclusions

We have presented observations of wave-coherent pressure work in the wave-affected atmospheric boundary layer. Observations are qualitatively consistent with existing wind-wave growth rate parameterizations, and a vertical decay that depends on height and surface wavenumber. The vertical decay is roughly consistent with $\exp(-2kz)$, although we recognize that this form of the vertical decay function is an imperfect approximation. The agreement between measured pressure work and existing models is seen in cospectra and in a frequency-integrated time series. The simple model for atmospheric work tends to overpredict the measured pressure work by a factor of 20%–50%; however, this is generally within the reported error bounds of a coefficient for the wave growth parameterizations, and this disagreement was smaller at higher wind speeds. At rapidly decreasing winds, upward pressure work fluxes were observed from waves traveling faster than winds.

Future work is needed to understand the impact of wave coherent pressure work on MO similarity and bulk flux formulae at high winds. For the specific instrument heights and wave states in this study, measurements indicate the TKE budget (and therefore MO similarity functions by proxy) start to be modified by waves at winds above 10–12 m s^{-1}. We feel that this problem has a particular relevance given the growing interest in using low-lying anemometers on autonomous platforms at sea for measurements in high winds.

Acknowledgments. This work was funded by NSF Award 2023020. Additional support was provided by Grants NSF 2316818, NASA 80NSSC21K0832, and ONR N00014-22-1-2405. Jay Sisson and Steve Faluotico helped design, deploy, maintain, and recover the tower and associated measurement systems. Thanks to Jonah Mikutowicz and the AGM and 41° North crews for invaluable help with deployment and recovery of the tower. Jim Wilczak provided the static pressure heads used in this experiment. Two anonymous reviewers provided feedback on an initial draft, and Al Plueddemann, Tim Duda, Chris Zappa, Alejandro Cifuentes-Lorenzen, and Roger Samelson provided helpful comments and discussions.

Data availability statement. Data used in this work (Zippel et al. 2022) is available through the WHOI Open Access Server (WHOAS) at https://doi.org/10.26025/1912/29583.

APPENDIX A

Estimation of the Miles' Parameter for Determining the Wind/Wave Energy Input

The Janssen (1991) wind input formulation is

$$\beta(f,\,\theta) = B\,\frac{\rho_a}{\rho_w}\,\frac{u_*^2}{c^2}\,\omega\cos^2(\theta), \tag{A1}$$

which depends on the Miles' parameter B. We follow the description in Komen et al. [1996, Eqs. (3.38)–(3.47) therein]. Parameter B is defined as

$$B = \frac{B_m}{\kappa^2}\,\mu\ln^4(\mu), \quad \mu \le 1, \tag{A2}$$

where $B_m = 1.2$ is a constant and μ is defined as

$$\mu = \left(\frac{u_*}{\kappa c}\right)^2 \Omega_m \exp[\kappa(u_*/c)\cos(\theta_r)], \tag{A3}$$

with $\Omega_m = \kappa^2 g z_0 u_*^{-2}$. The roughness length z_0 is defined with a Charnock relation,

$$z_0 = \hat{\alpha}\,\frac{\tau}{g}\left(1 - \frac{\tau_w}{\tau}\right)^{-1/2}, \tag{A4}$$

with τ_w being the stress from surface gravity waves. This stress is defined using the initial growth rate,

$$\tau_w = \int\int \frac{\beta(f,\,\theta)}{c}\,E(f,\,\theta)d\theta\,df. \tag{A5}$$

Calculation of B then requires the full growth rate, and must be done iteratively. We used an initial estimate of growth rate following Eq. (6) to solve for the wave stress, which was used to recompute the growth rate. We used a fixed number of iterations, 3, which served as a balance between computational speed and accuracy.

APPENDIX B

Estimation of Wave-Coherent and -Incoherent Spectra

The measured pw cospectra are decomposed using the assumption of a linear spectral model which is described here. This method closely follows Bendat and Piersol (2011, section 6.2.2 "Single-Input/Multiple-Output Model"), as well as Veron et al. (2008) and Grare et al. (2013a), in which the authors use a similar decomposition. Here, we assume that the time series of p' and w' each have a wave-coherent component, $\tilde{p}$ and $\tilde{w}$, that have a linear relationship with sea surface elevation η, such that the Fourier transform $\mathcal{F}\{\cdot\}$ of each measured time series can be expressed:

$$\mathcal{F}\{p'\} = \mathcal{F}\{p'_t + \tilde{p}\} = \mathcal{F}\{p'_t\} + H_p\mathcal{F}\{\eta\}, \tag{B1}$$

$$\mathcal{F}\{w'\} = \mathcal{F}\{w'_t + \tilde{w}\} = \mathcal{F}\{w'_t\} + H_w\mathcal{F}\{\eta\}, \tag{B2}$$

where $\mathcal{F}\{\tilde{p}\} = H_p\mathcal{F}\{\eta\}$ and $\mathcal{F}\{\tilde{w}\} = H_w\mathcal{F}\{\eta\}$ define the wave-coherent components, p'_t and w'_t are the wave-incoherent components, and H_p and H_w are complex transfer functions that depend on frequency. Here we use notation consistent with the measured time series, but note that the notation of Bendat and Piersol (2011) would equate to $\eta = x(t)$, $p' = y_1(t)$, and $w' = y_2(t)$, and use G_{xx} to denote the power spectrum of x, and G_{xy_1} to denote the complex cross-spectrum of x and y_1. Following Bendat and Piersol's (2011) Eq. (6.77), the complex transfer functions are defined using cross-spectra and autospectra,

$$H_p = \frac{G_{p\eta}(f)}{G_{\eta\eta}(f)}, \quad H_w = \frac{G_{w\eta}(f)}{G_{\eta\eta}(f)}, \tag{B3}$$

where $G_{p\eta}(f)$ is the complex cross-spectrum of p' and η, $G_{w\eta}(f)$ is the complex cross-spectrum of w' and η, and $G_{\eta\eta}(f)$ is the real-valued power spectrum of η.

The cross-spectrum between p' and w', assuming no wave-turbulent correlations (e.g., $\langle\tilde{p}p'_t\rangle = 0$, $\langle\tilde{p}w'_t\rangle = 0$, etc.), is then

$$\underbrace{G_{pw}(f)}_{\text{Total } pw} = \underbrace{H_p^*(f)H_w(f)G_{\eta\eta}(f)}_{\text{Wave-coherent } pw} + \underbrace{G_{p_{t'}w_{t'}}(f)}_{\text{Turbulent } pw}. \tag{B4}$$

Since only the real component of pw correlations contribute to the TKE equation, the wave-coherent pw spectrum is estimated combining Eqs. (B3) and (B4),

$$\mathrm{Re}\{G_{\tilde{p}\tilde{w}}(f)\} = \mathrm{Re}\{H_p^*(f)H_w(f)G_{\eta\eta}(f)\} = \frac{|G_{p\eta}||G_{w\eta}|}{G_{\eta\eta}}\cos(\Phi_{p\eta} - \Phi_{w\eta}), \tag{B5}$$

where $\Phi_{pw} = \arctan(\mathrm{Im}\{G_{pw}\}/\mathrm{Re}\{G_{pw}\})$ is the spectral phase. The wave-incoherent part $G_{p_{t'}w_{t'}}(f)$ is found using Eqs. (B4) and (B5). Here, we followed from Bendat and Piersol (2011), however Eq. (B5) can also be seen as analogous to Grare et al.'s (2013a) Eq. (17), which was formed for wave-coherent stress. We also note that Eq. (B5) can be reformed using magnitude squared coherence and autospectra, with magnitude squared coherence defined as $\gamma^2_{xy} = |G_{xy}|^2/(G_{xx}G_{yy})$.

The above formulation [Eq. (B5)] is consistent with previous efforts to measure the surface wave growth rate β from out-of-phase pressure $\mathrm{Im}\{G_{p\eta}\}$ (Hare et al. 1997; Donelan et al. 2006). Assuming a boundary condition where the atmospheric velocity equals the wave orbital motion at $z = 0$, we have $|G_{w\eta}(z = 0)| = \omega G_{\eta\eta}$ and $\Phi_{w\eta}(z = 0) = 90$. Combining with Eq. (B5),

$$\mathrm{Re}\{G_{\tilde{p}\tilde{w}}(f,\,z = 0)\} = \frac{|G_{p\eta}|\omega G_{\eta\eta}}{G_{\eta\eta}}\cos(\Phi_{p\eta} - 90), \tag{B6}$$

which can be reduced to

$$\mathrm{Re}\{G_{\tilde{p}\tilde{w}}(f,\,z = 0)\} = \omega|G_{p\eta}|\sin(\Phi_{p\eta}). \tag{B7}$$

Using trig identities for phase, $|G|\sin(\Phi) = \mathrm{Im}\{G\}$, such that,

$$\mathrm{Re}\{G_{\tilde{p}\tilde{w}}(f,\,z = 0)\} = \omega\,\mathrm{Im}\{G_{p\eta}\}. \tag{B8}$$

APPENDIX C

Errors in Estimates of Spectral Phase

Time and space offsets in measurements can cause spectral phase estimates to vary in frequency. For phases of the form $\Phi = \mathbf{k} \cdot \mathbf{x} - \omega t + \phi$, time offsets result in linear change in phase with frequency, $\Delta\Phi = -\omega\Delta t$, and space offsets result in a change of phase, $\Delta\Phi = \mathbf{k} \cdot \Delta\mathbf{x}$, with time and space offsets Δt and $\Delta\mathbf{x}$, respectively. In this dataset, time delays were determined to be small on average resulting in minimal functional bias in phase estimates. Spatial offsets between atmospheric pressure and velocity were also determined to be relatively small at the frequencies of interest, typically resulting in directional phase shifts less $\Delta\Phi < 5°$. However, there was some uncertainty regarding the spatial location of the lidar spot on the surface. While the instrument's dot was aligned prior to deployment of the tower, small rotations and offsets resulting during the deployment yield some uncertainty in the final horizontal position of the η measurement. Therefore, phases $\Phi_{\eta p}$ and $\Phi_{\eta w}$ are expected to have larger uncertainty due to unknown space offsets $\Delta\mathbf{x}_{\eta p}$ and $\Delta\mathbf{x}_{\eta w}$. Assuming deep water dispersion, the resulting phase bias would depend on frequency squared and wave direction. In practice, this bias is small at frequencies near $f_{\max}$ where both wave energy and pressure work fluxes tend to be largest. No realistic time/space offsets could explain the measured $\Phi_{\eta p}$ near and just above $f_{\max}$. However, the steep increase in bias with frequency resulting from spatial offsets could plausibly explain the high-frequency phase $\Phi_{\eta p} > 180°$ in Fig. 5a during the high-wind event in May. It is important to note that this high-frequency bias is not reflected in the final wave-coherent pressure work estimate since the phase difference $\Phi_{\eta p} - \Phi_{\eta w}$ subtracts this unknown offset, since $\Delta\mathbf{x}_{\eta p} - \Delta\mathbf{x}_{\eta w} = \Delta\mathbf{x}_{pw}$. This latter offset, $\Delta\mathbf{x}_{pw}$, is known and is small.

REFERENCES

Ardhuin, F., B. Chapron, and F. Collard, 2009: Observation of swell dissipation across oceans. *Geophys. Res. Lett.*, **36**, L06607, https://doi.org/10.1029/2008GL037030.

——, and Coauthors, 2010: Semi-empirical dissipation source functions for ocean waves: Part I, definitions, calibration, and validations. *J. Phys. Oceanogr.*, **40**, 1917–1941, https://doi.org/10.1175/2010JPO4324.1.

Ayet, A., and B. Chapron, 2022: The dynamical coupling of wind-waves and atmospheric turbulence: A review of theoretical and phenomenological models. *Bound.-Layer Meteor.*, **183**, 1–33, https://doi.org/10.1007/s10546-021-00666-6.

Belcher, S., and J. Hunt, 1993: Turbulent shear flow over slowly moving waves. *J. Fluid Mech.*, **251**, 109–148, https://doi.org/10.1017/S0022112093003350.

Bendat, J. S., and A. G. Piersol, 2011: *Random Data: Analysis and Measurement Procedures*. 4th ed. John Wiley and Sons, 613 pp.

Buckley, M., F. Veron, and K. Yousefi, 2020: Surface viscous stress over wind-driven waves with intermittent airflow separation. *J. Fluid Mech.*, **905**, A31, https://doi.org/10.1017/jfm.2020.760.

Cifuentes-Lorenzen, A., J. B. Edson, and C. J. Zappa, 2018: Air–sea interaction in the southern ocean: Exploring the height of the wave boundary layer at the air–sea interface. *Bound.-Layer Meteor.*, **169**, 461–482, https://doi.org/10.1007/s10546-018-0376-0.

Donelan, M. A., A. V. Babanin, I. R. Young, M. L. Banner, and C. McCormick, 2005: Wave-follower field measurements of the wind-input spectral function. Part I: Measurements and calibrations. *J. Atmos. Oceanic Technol.*, **22**, 799–813, https://doi.org/10.1175/JTECH1725.1.

——, ——, ——, and ——, 2006: Wave-follower field measurements of the wind-input spectral function. Part II: Parameterization of the wind input. *J. Phys. Oceanogr.*, **36**, 1672–1689, https://doi.org/10.1175/JPO2933.1.

Edson, J., and Coauthors, 2007: The coupled boundary layers and air–sea transfer experiment in low winds. *Bull. Amer. Meteor. Soc.*, **88**, 341–356, https://doi.org/10.1175/BAMS-88-3-341.

Edson, J. B., and C. Fairall, 1998: Similarity relationships in the marine atmospheric surface layer for terms in the TKE and scalar variance budgets. *J. Atmos. Sci.*, **55**, 2311–2328, https://doi.org/10.1175/1520-0469(1998)055<2311:SRITMA>2.0.CO;2.

——, ——, P. Mestayer, and S. Larsen, 1991: A study of the inertial-dissipation method for computing air-sea fluxes. *J. Geophys. Res.*, **96**, 10 689–10 711, https://doi.org/10.1029/91JC00886.

——, and Coauthors, 2013: On the exchange of momentum over the open ocean. *J. Phys. Oceanogr.*, **43**, 1589–1610, https://doi.org/10.1175/JPO-D-12-0173.1.

Grachev, A., and C. Fairall, 2001: Upward momentum transfer in the marine boundary layer. *J. Phys. Oceanogr.*, **31**, 1698–1711, https://doi.org/10.1175/1520-0485(2001)031<1698:UMTITM>2.0.CO;2.

Grare, L., 2009: Étude des interactions océan-atmosphère à proximité immédiate de l'interface: Application aux vagues de vent et aux vagues extrêmes. Ph.D. thesis, Université de la Méditerranée-Aix-Marseille II, 241 pp.

——, L. Lenain, and W. K. Melville, 2013a: Wave-coherent airflow and critical layers over ocean waves. *J. Phys. Oceanogr.*, **43**, 2156–2172, https://doi.org/10.1175/JPO-D-13-056.1.

——, W. L. Peirson, H. Branger, J. W. Walker, J.-P. Giovanangeli, and V. Makin, 2013b: Growth and dissipation of wind-forced, deep-water waves. *J. Fluid Mech.*, **722**, 5–50, https://doi.org/10.1017/jfm.2013.88.

——, L. Lenain, and W. K. Melville, 2018: Vertical profiles of the wave-induced airflow above ocean surface waves. *J. Phys. Oceanogr.*, **48**, 2901–2922, https://doi.org/10.1175/JPO-D-18-0121.1.

Hanley, K. E., and S. E. Belcher, 2008: Wave-driven wind jets in the marine atmospheric boundary layer. *J. Atmos. Sci.*, **65**, 2646–2660, https://doi.org/10.1175/2007JAS2562.1.

Hare, J. E., T. Hara, J. B. Edson, and J. M. Wilczak, 1997: A similarity analysis of the structure of airflow over surface waves. *J. Phys. Oceanogr.*, **27**, 1018–1037, https://doi.org/10.1175/1520-0485(1997)027<1018:ASAOTS>2.0.CO;2.

Harris, D. L., 1966: The wave-driven wind. *J. Atmos. Sci.*, **23**, 688–693, https://doi.org/10.1175/1520-0469(1966)023<0688:TWDW>2.0.CO;2.

Herbers, T. H. C., P. F. Jessen, T. T. Janssen, D. B. Colbert, and J. H. MacMahan, 2012: Observing ocean surface waves with GPS-tracked buoys. *J. Atmos. Oceanic Technol.*, **29**, 944–959, https://doi.org/10.1175/JTECH-D-11-00128.1.

Hristov, T., and J. Ruiz-Plancarte, 2014: Dynamic balances in a wavy boundary layer. *J. Phys. Oceanogr.*, **44**, 3185–3194, https://doi.org/10.1175/JPO-D-13-0209.1.

Hristov, T. S., S. D. Miller, and C. A. Friehe, 2003: Dynamical coupling of wind and ocean waves through wave-induced air flow. *Nature*, **422**, 55–58, https://doi.org/10.1038/nature01382.

Janssen, P. A., 1989: Wave-induced stress and the drag of air flow over sea waves. *J. Phys. Oceanogr.*, **19**, 745–754, https://doi.org/10.1175/1520-0485(1989)019<0745:WISATD>2.0.CO;2.

——, 1991: Quasi-linear theory of wind-wave generation applied to wave forecasting. *J. Phys. Oceanogr.*, **21**, 1631–1642, https://doi.org/10.1175/1520-0485(1991)021<1631:QLTOWW>2.0.CO;2.

——, 1999: On the effect of ocean waves on the kinetic energy balance and consequences for the inertial dissipation technique. *J. Phys. Oceanogr.*, **29**, 530–534, https://doi.org/10.1175/1520-0485(1999)029<0530:OTEOOW>2.0.CO;2.

——, and J.-R. Bidlot, 2023: Wind-wave interaction for strong winds. *J. Phys. Oceanogr.*, **53**, 779–804, https://doi.org/10.1175/JPO-D-21-0293.1.

Jeffreys, H., 1925: On the formation of waves by wind. *Proc. Roy. Soc. London*, **107A**, 189–206, https://doi.org/10.1098/rspa.1925.0015.

——, 1926: On the formation of waves by wind. II. *Proc. Roy. Soc. London*, **110A**, 341–347, https://doi.org/10.1098/rspa.1926.0014.

Komen, G. J., L. Cavaleri, M. Donelan, K. Hasselmann, S. Hasselmann, and P. Janssen, 1996: *Dynamics and Modelling of Ocean Waves*. Cambridge University Press, 532 pp.

Kudryavtsev, V., V. Makin, and J. Meirink, 2001: Simplified model of the air flow above waves. *Bound.-Layer Meteor.*, **100**, 63–90, https://doi.org/10.1023/A:1018914113697.

Miles, J. W., 1957: On the generation of surface waves by shear flows. *J. Fluid Mech.*, **3**, 185–204, https://doi.org/10.1017/S0022112057000567.

Nishiyama, R. T., and A. J. Bedard Jr., 1991: A "quad-disc" static pressure probe for measurement in adverse atmospheres: With a comparative review of static pressure probe designs. *Rev. Sci. Instrum.*, **62**, 2193–2204, https://doi.org/10.1063/1.1142337.

Phillips, O. M., 1957: On the generation of waves by turbulent wind. *J. Fluid Mech.*, **2**, 417–445, https://doi.org/10.1017/S0022112057000233.

Plant, B., 1982: A relationship between wind stress and wave slope. *J. Geophys. Res.*, **87**, 1961–1967, https://doi.org/10.1029/JC087iC03p01961.

Snyder, R., F. Dobson, J. Elliott, and R. Long, 1981: Array measurements of atmospheric pressure fluctuations above surface gravity waves. *J. Fluid Mech.*, **102**, 1–59, https://doi.org/10.1017/S0022112081002528.

Thomson, J., J. B. Girton, R. Jha, and A. Trapani, 2018: Measurements of directional wave spectra and wind stress from a wave glider autonomous surface vehicle. *J. Atmos. Oceanic Technol.*, **35**, 347–363, https://doi.org/10.1175/JTECH-D-17-0091.1.

Veron, F., W. K. Melville, and L. Lenain, 2008: Wave-coherent air–sea heat flux. *J. Phys. Oceanogr.*, **38**, 788–802, https://doi.org/10.1175/2007JPO3682.1.

Wu, J., S. Popinet, and L. Deike, 2022: Revisiting wind wave growth with fully coupled direct numerical simulations. *J. Fluid Mech.*, **951**, A18, https://doi.org/10.1017/jfm.2022.822.

Yelland, M., P. Taylor, I. Consterdine, and M. Smith, 1994: The use of the inertial dissipation technique for shipboard wind stress determination. *J. Atmos. Oceanic Technol.*, **11**, 1093–1108, https://doi.org/10.1175/1520-0426(1994)011<1093:TUOTID>2.0.CO;2.

Young, I., 1999: *Wind Generated Ocean Waves*. Elsevier Ocean Engineering Book Series, Vol. 2, Elsevier, 287 pp.

Zippel, S. F., J. B. Edson, M. E. Scully, and O. R. Keefe, 2022: Data to accompany "Direct observation of wave-coherent pressure work in the atmospheric boundary layer." MBLWHOI Library, accessed 29 November 2023, https://doi.org/10.26025/1912/29583.